Deep-learning-based Compliant Motion Control of a Pneumatically-driven Robotic Catheter

Di Wu, Xuan Thao Ha, Yao Zhang, Mouloud Ourak, Gianni Borghesan, Kenan Niu, Fabian Trauzettel, Jenny Dankelman, Arianna Menciassi and Emmanuel Vander Poorten

***Abstract*—In cardiovascular interventions, when steering catheters and especially robotic catheters, great care should be paid to prevent applying too large forces on the vessel walls as this could dislodge calcifications, induce scars or even cause perforation. To address this challenge, this paper presents a novel compliant motion control algorithm that relies solely on position sensing of the catheter tip and knowledge of the catheter's behavior. The proposed algorithm features a data-driven tip position controller. The controller is trained based on a so-called *control Long Short-Term Memory Network* (control-LSTM). Trajectory following experiments on four different trajectories are conducted to validate the quality of the proposed control-LSTM. Results demonstrated superior positioning capability with sub-degree precision of the new approach in the presence of severe rate-dependent hysteresis. Experiments both in a simplified setup as well as in an aortic phantom further show that the proposed approach allows reducing the interaction forces with the environment by around 70%. This work shows how deep learning can be exploited advantageously to avoid tedious modeling that would be needed to precisely steer continuum robots in constrained environments such as the patient's vasculature.**

***Index Terms*—robotic catheter, compliant motion control, hysteresis, LSTM, pneumatic artificial muscle.**

I. INTRODUCTION

Cardiac catheterization is a popular minimally invasive procedure to treat cardiovascular conditions. During catheterization, a catheter is inserted by an interventional cardiologist into a heart chamber or vessel for diagnostic or therapeutic purposes. In such a procedure, conventional steerable catheters are commonly used, which are steered manually. Because the vessel geometry is complex, and the catheter is deformable and exhibits hysteresis, a high level of expertise is required to safely navigate catheters through the narrow and tortuous vessels. A robotic catheter is a steerable catheter of which one or more of the degrees of freedom (DOF) can be commanded in a computer-controller fashion. The robotic catheter could potentially improve current procedure [1], which is demonstrated by several commercially available robotic catheter systems emerging in recent years such as the Sensei® and Magellan™ (Hansen/Auris Medical, Inc., USA), Monarch® (Auris Health Inc., USA), or CorPath® (Corindus Inc., USA).

However, modeling and actively steering robotic catheters remain challenging. This complexity stems from the fact that the catheter configuration depends both on steering maneuvers and on a complex distributed interaction with the environment. Managing the interaction force between catheter and surrounding anatomy to an acceptable level is crucial to avoid tissue damage. Especially the interaction at the tip is important, as this is the most acute part of the catheter that could easily pierce tissue or dislodge calcification. Distributed forces along the catheter body could rise as well, e.g. if the tip is blocked somehow. However, as we observed that the effect of lateral distributed forces over the catheter body is less risky than tip point forces, we will deal with the former in future works.

If the configuration, i.e. the pose and/or shape, of the catheter's steerable segments could be measured, such information could be used advantageously to control the catheter such that it could be steered in a more gentle fashion through a vessel. Several methods have been proposed in the literature to achieve this goal. Kesner *et al.* presented a method in which a force sensor was integrated in the tip of a robotic catheter to minimize tip interaction force [2]. This method requires a dedicated force sensor, which limits the functionalization of the catheter as there will be limited room left for integrating other functions. Also, the catheter's structural properties may be negatively affected by such force sensor. Other approaches make use of the complicated nonlinear mechanical models to achieve compliant motion control [3], [4]. Said models are typically very specific to the robotic structure at hand. Furthermore, significant modeling efforts are needed to obtain a very precise characterization of the input-output behavior of a specific continuum robot. To circumvent complex and time-consuming modeling, model-less control methods have been investigated in the past. A Multiagent Deep Q Network (MADQN), based on reinforcement learning, was employed by Ji *et al.* to control a cable-driven continuum surgical robot [5]. Yip *et al.* proposed a model-less controller based on a real-time estimated Jacobian of the continuum manipulator [6]. Follow-up work by Yip *et al.* further developed a hybrid position/force controller enabling safe interactions with the unknown constrained environment [7]. However, this model-less method relies on a dedicated

This work was supported by the ATLAS project. This project has received funding from the European Union's Horizon 2020 research and innovation program under the Marie Sklodowska-Curie grant agreement No. 813782. *(D. Wu and X.T. Ha contributed equally to this work.) (Corresponding author: Di Wu)*

D. Wu and F. Trauzettel are with the Department of Mechanical Engineering, KU Leuven, Belgium, and also with the Faculty of 3mE, TU Delft, the Netherlands. (email: di.wu@kuleuven.be, f.trauzettel@tudelft.nl)

X.T. Ha is with the Department of Mechanical Engineering, KU Leuven, Belgium, and also with The BioRobotics Institute, Scuola Superiore Sant'Anna, Italy. (email: xuanthao.ha@kuleuven.be)

Y. Zhang, M. Ourak, K. Niu and E. Vander Poorten are with the Department of Mechanical Engineering, KU Leuven, Belgium. (email: yao.zhang@kuleuven.be; mouloud.ourak@kuleuven.be; kenan.niu@kuleuven.be; emmanuel.vanderpoorten@kuleuven.be)

G. Borghesan is with the Department of Mechanical Engineering, KU Leuven, Belgium, and also with Flanders Make, Belgium. (email: gianni.borghesan@kuleuven.be)

J. Dankelman is with the Faculty of 3mE, TU Delft, the Netherlands. (email: J.Dankelman@tudelft.nl)

A. Menciassi is with The BioRobotics Institute, Scuola Superiore Sant'Anna, Italy. (email: arianna.menciassi@santannapisa.it)

Digital Object Identifier (DOI): see top of this page.

distal force sensor and requires an excellent accuracy of that sensor. No matter the approach, whether model-based or model-less, additional complexity stems from the non-ideal behavior of the actuator and the transmission system where phenomena such as friction, hysteresis, or backlash present additional challenges to control the continuum robots [8], [9]. Reliable compliant motion control, therefore, requires accounting for both robot kinematics and the said inherent non-linear behavior. Compared to previous works, the proposed method aims to learn all these aspects in one shot.

Hysteresis can be compensated by closed-loop control using Electromagnetic (EM) sensing [10], optical trackers [11] or medical imaging [12]. Alternatively, hysteresis can also be compensated in open-loop using feed-forward analytical models [13]–[15]. Open-loop approaches are appealing as they eliminate the need for installing sensors in the distal end. However, creating reliable analytic models often require tedious identificantion procedures. Next, if possible, the identified analytical model somehow needs to be inverted.

Deep learning (DL), albeit being a black-box method, have gained growing attention due to their ability to accurately represent complex nonlinear behavior. Traditional Machine Learning (ML) or DL methods were investigated in the past to model continuum robots. In [8], a neural network to estimate the cable tension of a continuum robot in unloaded motion was developed. Porto *et al.* proposed to use an Extreme Learning Machine, a supervised learning method, to model the inverse kinematics of a flexible endoscope and realise 3D position control [16]. Three data-driven approaches were proposed by Xu *et al.* to learn the inverse kinematics of a flexible surgical manipulator [17]. These approaches were validated by a trajectory tracking experiment. Among three approaches, the K-nearest neighbors regression achieved the lowest Root Mean Square Error (RMSE) of 2.1275 mm. Both studies [16], [17] focused on cable-driven robots, and adopted traditional ML methods e.g. regression, but did not investigate the benefit of the latest advancements in DL. Our previous research [18] used an LSTM to *model* the hysteresis of a catheter with sub-degree precision of the tip bending angle. On the other hand, this paper proposes an open-loop controller based on a dedicated LSTM, which is different from the modeling LSTM of [18]. In this work, the LSTM is used to *control and compensate* for the hysteresis in a catheter. In order to distinguish it from the LSTM of [18], the LSTM in this paper is referred to as *control-LSTM*. The control-LSTM, which basically is a free-space position controller, forms the basis for the proposed compliant motion control algorithm. In practice, the LSTM-based controller will react to external forces by moving the catheter tip position to a pose that reduces the force acting at the tip. In summary, the main contributions of this work are:

- an open-loop controller based on an LSTM to control and compensate for the hysteresis in a catheter system. The proposed control-LSTM is used as a feedforward free-space catheter controller robust to severe hysteresis. It is precise and has a simple training procedure. Moreover, the control-LSTM does not require a separate inversion step to be used in a controller as would be needed by most traditional analytical hysteresis models such as [19].

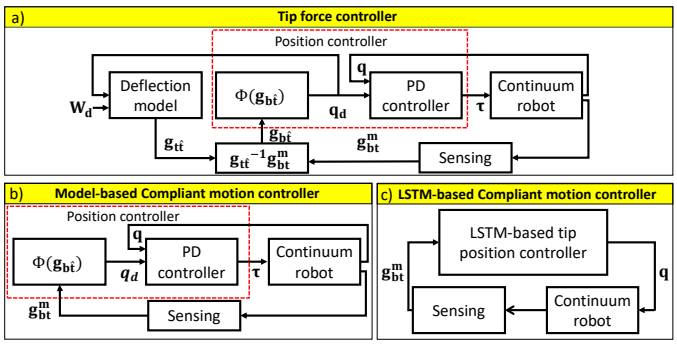

Figure 1. Different tip force controllers: a) block diagram of a tip force controller; b) a simplified version of a) to achieve compliant motion control. In the compliant motion controller, the desired tip wrench W_d is set to $O^{6\times1}$, which makes $\boldsymbol{g_{t\hat{t}}}$ become identity matrix; c) The block diagram of the proposed LSTM-based compliant motion controller.

- a compliant motion controller based on the developed control-LSTM position controller that uses pose sensing as input without needing force- or contact-sensing and without sensing actuator torques.
- validation of the proposed controller both in a simplified setup as well as in an aortic phantom.

The rest of the paper is organized as follows: Section II introduces some basic formulations of the compliant motion control as well as the concept of DL-based compliant motion control. Section III details the experimental setup, the collection of training data and the structure of the control-LSTM. Section IV describes the trajectory following experiments. Next, the validation of the compliant motion control is displayed in Section V and Section VI. Section VII concludes the paper.

II. DL-BASED COMPLIANT MOTION CATHETER CONTROL

The basic formulations for tip force control of continuum robots are briefly discussed in Sec. II-A. A new DL method that enables compliant motion control, and at the same time capturing the non-ideal behaviour of the employed catheter, is introduced in Sec. II-B.

A. Tip force control of continuum robots

Kinematics for continuum robots has been studied in the literature [20]. The backbone of a continuum robot can be represented by a space curve $\mathbf{p}(\mathbf{q}, s) \in \mathbb{R}^3$ which is a function of n input kinematic variables $\mathbf{q} \in \mathbb{R}^n$ and the arc length $s \in [0, l]$, with coordinate frames defined at the base (B) and the tip (T and $\hat{T}$) [3]. In this work, the tip frame $\hat{T}$, is used to describe the configuration of the tip in an unloaded condition while T corresponds to the tip configuration upon application of an external tip wrench $\mathbf{W} \in \mathbb{R}^6$ e.g. due to environmental contact. A rigid body transformation $\mathbf{g_{bi}(q)}$ is used to describe the configuration frame I of each point along the robot's backbone relative to base frame B. The configuration of tip frame T can be described in the base frame B as follows:

$$\mathbf{g_{bt}(q, W)} = \mathbf{g_{b\hat{t}}(q) g_{\hat{t}t}(q, W)}. \tag{1}$$

Assuming that it is desired to apply an external wrench $\mathbf{W_d}$ at the tip of a continuum robot while maintaining the tip at a configuration $\mathbf{g^m_{bt}}$. Then, the measured tip configuration $\mathbf{g^m_{bt}}$, desired tip wrench $\mathbf{W_d}$ and the desired actuator input variable $\mathbf{q_d}$ are relate as:

$$\mathbf{g_{bt}^m} = \mathbf{g_{b\hat{t}}}(\mathbf{q_d})\mathbf{g_{\hat{t}t}}(\mathbf{q_d}, \mathbf{W_d}). \quad (2)$$

If the model is correct for an actuation $\mathbf{q_d}$, the continuum robot would be deformed and the desired tip wrench $\mathbf{W_d}$ would be produced accordingly. Given the mechanical properties of the continuum robot, $\mathbf{g_{\hat{t}t}}(q, W)$ can be solved efficiently using the method presented by Mahvash *et al.* [3]. The kinematic mapping can then be used to control the tip wrench. In other words, a position controller can be used to solve the inverse kinematic problem and drive the actuators to:

$$q_d = \Phi(\mathbf{g_{b\hat{t}}}(q_d)) = \Phi(\mathbf{g_{t\hat{t}}^{-1}}(q_d, W_d)\mathbf{g_{bt}^m}). \quad (3)$$

where $\Phi(.)$ is a multidimensional inverse kinematic function describing the continuum robot in an unloaded condition. The block diagram of the tip force controller can be seen in Fig. 1a. The sensing block measures the tip configuration and provides feedback to the controller. The deflection model helps computing the continuum robot's deformation for a given input kinematic variable and desired external tip wrench. Nevertheless, as explained in the next section, the derivation of such deflection model falls outside the scope of this paper. Readers are referred to [3] for details on a deflection model of continuum robot.

The aim of compliant motion control is to minimize the force applied to the robot tip ($\mathbf{W_d} = \mathbf{0^{6\times1}}$). This makes the output of the deflection model $\mathbf{g_{t\hat{t}}}$ become equal to the identity matrix ($\mathbf{g_{t\hat{t}}} = \mathbf{I^{4\times4}}$). A simplified version of the original tip force controller used for the compliant motion control algorithm will be described in the next subsection.

B. Compliant motion control algorithm

The objective of our proposed compliant motion controller, as can be seen in Fig. 1b, is to advance the robot's tip to the position provided by the sensing block and thus, minimize the force applied to the tip. To overcome the problem of hysteresis in cable- or fluidics-driven catheters, instead of using the traditional kinematic model-based method [21] to control the catheter tip position, a control-LSTM position controller (hereinafter referred as "LSTM controller") was implemented to control the catheter tip position. The control-LSTM can predict the actuator commands that can advance the catheter tip to an conformed position, where the interaction force is minimized. This approach helps reduce effort in modeling the complex nonlinear behavior and simplified the identification procedure of catheters. Moreover, the proposed LSTM compliant motion controller requires only one position tracking sensor to measure tip position. The block diagram of the proposed LSTM-based compliant motion controller is shown in Fig. 1c.

Details on control-LSTM training and validation are going to be described in Sec. III and Sec. IV. The overall block diagram of LSTM compliant motion controller is shown in Fig. 2. Note that the proposed methods can be generalized to other sensors that are able to provide real-time estimates of the catheter's tip pose such as fluoroscopy [22], Electrical impedance tomography [23], bending resistance [24] or Fiber Bragg Grating-based shape sensing method [25], [26]. However, in this work, the EM tracker serves as a candidate that can track tip position in order to enable compliant motion control.

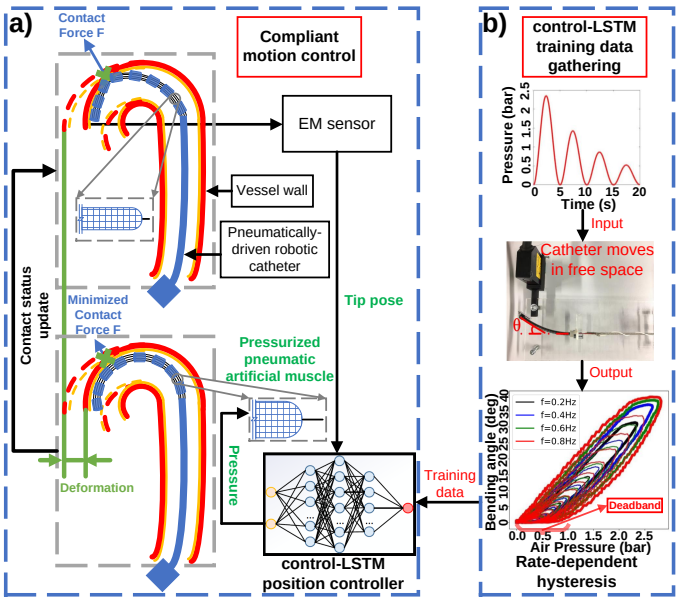

Figure 2. Overview of the compliant motion control algorithm: (a) Only tip pose information was acquired and then was input into the control-LSTM. The pressure predicted by the control-LSTM advances the catheter to a proper position where the interaction force is minimized. (b) Training data for the control-LSTM were collected when catheter moved in free space.

III. Experimental Setup and LSTM Training

A. Experimental Setup for validating the control-LSTM

This work uses a catheter system actuated by Pneumatic Artificial Muscles (PAMs). A motivation for this actuation can be found in [27]. Nevertheless, PAM-driven catheter system suffer from rate-dependent hysteresis [19].

A bench-top setup has been built for experimental validation. The setup contains a 85 mm long distal catheter segment with a diameter of 4.4 mm. The segment consists of a Nitinol notched-tube backbone. These notches make the catheter bendable in 2 DOFs [27]. In this work, the algorithm was validated in 1 DOF, while expanding this algorithm to 2-DOF will be part of our future work. A PAM is connected off-center by a steel cable to the catheter tip. By inflating the PAM, the PAM contracts. The resulting cable tension exerts a torque on the catheter tip making it bend side-ways. A proportional pressure valve (Festo Corporation, Germany) is employed to regulate the pressure in the PAM. A laser distance sensor (OADM 12I6460/S35A, Baumer Group, Switzerland) or an EM tracker (Northern Digital Inc., Canada) is used to measure the catheter tip motion. For more details regarding the catheter system please refer to [18]. Figure 2b (bottom, right) shows the rate-dependent, saturated and asymmetric hysteresis of the PAM-driven catheter. The deadband pressure is about 0.7 bar. The rate-dependent hysteresis offsets range from 0.3 bar to 1.2 bar, as the frequency increases from 0.2 Hz to 0.8 Hz.

B. Training Data Acquisition

The training data were collected when the catheter bends in 1 DOF. To generate abundant training data, descending sinusoidal pressure patterns with zero baseline following (4) and with non-zero baseline, along (5), were sent to the catheter.

$$p_1(t) = Ae^{-\tau t}(\sin(2\pi ft - \frac{\pi}{2}) + 1) \qquad [\text{bar}] \qquad (4)$$

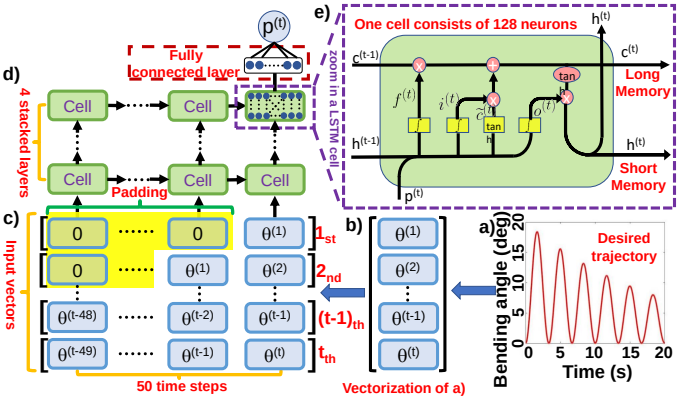

Figure 3. Inputs and structure of the control-LSTM (a)-(c): the trajectory is transformed into 50×1 long vectors that serve as input for the control-LSTM; (d)-(e) a stacked 4-layer control-LSTM that consists of LSTM cells, is unrolled into multiple time steps.

$$p_2(t) = Ae^{-\tau t}(\sin(2\pi f t - \frac{\pi}{2})) + A \qquad \text{[bar]} \qquad (5)$$

These signals generated the multi-loop hysteresis (Fig. 2b). To achieve a maximum pressure of 3 bars, the amplitude A is set to 1.5 bar. The variable f represents the excitation frequency (Hz). The time constant τ controls the rate at which the pressure rises or falls. This work only investigates the case where the frequency is less than 1 Hz. Figure 2b demonstrates that the formation of the hysteresis is affected not only by the frequency but also by the pressure amplitude. Therefore, different frequencies and pressure amplitudes are combined to excite the catheter system. The frequency f was switched between 0.2, 0.4, 0.6, 0.8, while τ was chosen as 0.02, 0.05, 0.1, 0.15, 0.2. Combining these two variables as well as the signals from (4) and (5) resulted in 40 groups of training data. Measurements were sampled at 250 Hz (laser sensor), producing a training data set of 260269 samples in total.

In training, the bending angle is input of the control-LSTM. The pressure, the parameter to be learned, was the output. Note that the control-LSTM's learning process is not straightforward. This is because the training data that is collected is somewhat idealised. During training, the input data (the bending angle) are noisy (due to measurement sensor noise) and exhibit a hysteretic behavior, while the outputs are 'clean' perfect sinusoidal pressure setpoints. Conversely, in practice, the control-LSTM will typically be provided with "clean" bending angle motion commands and is asked to predict the associated hysteretic pressure setpoints that would produce such smooth variations in bending angle. For this to work, the control-LSTM thus needs to be able to generalize and learn itself the patterns that do not exist in the training data.

C. Structure and hyperparameters of the control-LSTM

When a system exhibits hysteresis, the output of the system is not only determined by the current input, but also by historical inputs [28]. The LSTM's ability to learn historical information and use prior knowledge to predict system behavior at future time steps [29] formed a key motivation to use this network for this application. An LSTM can be viewed as a stack of LSTM cells (Fig. 3d), where each cell contains a number of units (Fig. 3e). Each LSTM cell is equipped with three gates i.e. an input gate i, an output gate o, and a forget gate f (Fig. 3e) that regulate the information flow [29].

Within this work, a 4-layer stacked control-LSTM (Fig. 3d) was used. The number of neurons in each cell was set to 128. These two parameters were derived from an ablation study. As shown in Table II, different numbers of hidden layers ranging from 2 to 5 layers with different combinations of neurons in each layer were tested. For each configuration, the control-LSTM was trained three times. The average validation losses, shown in Table II, were computed by averaging out the last 20% epochs (namely for 100 epochs, the average of $100 \times 20\% = 20$ loss values). By checking the result among multiple (in this case 3) training sessions and by averaging also the losses over epochs, the chance for an accidental outcome/error is reduced. The validation loss is the sum of the Mean Squared Error (MSE) of the predicted pressure (in bar) with respect to the ground truth. The combination of 4×128 produced the lowest average validation loss (0.00535) with moderate computational power, thus this configuration was chosen for the final control-LSTM structure. The pre-processing flow for the inputs into the control-LSTM is described as follows: a pre-defined trajectory is presented as a vector (Fig. 3b). The vector is split into multiple vectors with a length of 50 by means of a sliding window approach (Fig. 3c) as the inputs to the control-LSTM. The window size of 50 was found to balance well between model precision and computational cost [18]. As shown in the yellow highlighted area in Fig. 3c, zeros were padded on the left for the first 49 input vectors, when there are not enough historical values present yet. A fully connected layer (input dimensions = 128, output dimension =1) was added after the last LSTM cell. All the training data was normalized between [-1,1] to avoid large weights and to speed up the training procedure. The remaining hyperparameters of the control-LSTM are listed in Table I. The network was implemented using PyTorch. The training procedure was carried out on a 4 GB NVIDIA® CUDA-capable GPU. The control-LSTM was trained for 100 epochs until the control-LSTM was adequately optimized. The whole training duration took approximately 2.25 hours.

D. Implementation of the iDRDPI model

To assess the performance of the control-LSTM, an inverse Deadband Rate-Dependent Prandtl-Ishlinskii (iDRDPI) model, introduced in [19], was implemented for comparison. The iDRDPI model can compensate for hysteresis at different frequencies and also takes both major and minor loops into account. In addition, deadband operators in this model allow it to deal with deadzone that appears at the bottom of the hysteresis loops (see Fig. 2b). Therefore, the iDRDPI model is well suited to tackle rate-dependent, saturated and asymmetric hysteresis exhibited in the aforementioned catheter system. To identify the iDRDPI model, an inverse model of the Generalized Prandtl-Ishlinskii (GPI) was used, which provided a fairly accurate output for hysteresis compensation at a single frequency. The identification of the iDRDPI model in our work was divided into two steps: on the first step, four GPI models were identified by the hysteresis data at four frequencies i.e. 0.2, 0.4, 0.6, 0.8 (19635 data points in total), then four cor-

Table I
HYPERPARAMETERS FOR THE CONTROL-LSTM NETWORK

	Number of hidden layers	Number of neurons per cell	Activation functions	Optimizer	Loss function	Training-subset /Validation ratio	Batch size	Learning Rate	Epoches
control-LSTM	4	128	Tanh/Sigmoid	Adam	L2 Loss	70%/30%	16	0.001	100

Table II
RESULTS OF ABLATION STUDY

LSTM configuration		Avg. validation loss (bar^2)	Training time per epoch (s)
Batch size = 16	2 * 128	0.00924 (+72.71%)	65.46 (-39.70%)
	3 * 128	0.00638 (+19.25%)	88.34 (-18.63%)
	4 * 64	0.00672 (+25.61%)	100.00 (-7.86%)
	4 * 128	0.00535	108.56
	4 * 256	0.00563 (+5.23%)	122.87 (-11.65%)
	5 * 128	0.00784 (+46.54%)	130.64 (+20.33%)
4 * 128	Batch size = 8	0.00743 (+38.88%)	210.41 (+93.82%)
	Batch size = 32	0.01435 (+168.22%)	55.28 (-49.08%)

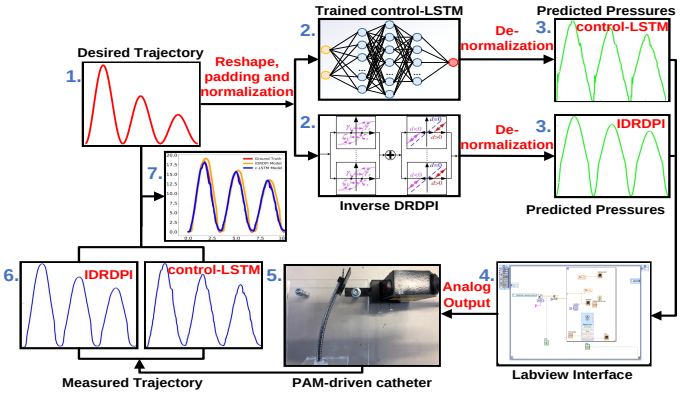

Figure 4. Experimental procedure to verify the performance of the control-LSTM and the iDRDPI model.

responding inverse GPI models could be obtained by directly inverting the previously obtained GPI model. The inverse GPI models were able to generate training data for the iDRDPI model. In the second step, the identified inverse GPI model generated 150000 virtual training data, which was used to train the iDRDPI model. The parameters of the iDRDPI model were identified based on a genetic algorithm in MATLAB® Toolbox. The identification process was performed on a CPU (Intel Corei7-7700 CPU @ 2.80GHz with a RAM of 8.00GB) as there was no widespread library for GPU-based training. The whole identification procedure of the iDRDPI model took around 3.5 hours. The iDRDPI model was trained for 300 iterations. The mean of the relative change in the last 20% of iterations was just 0.07% when the stop condition was triggered, which revealed that the model was fully converged. As shown in Fig. 4, the iDRDPI model was also validated using the same procedure as the control-LSTM.

IV. VALIDATION OF THE LSTM-BASED CONTROLLER

To evaluate the trained control-LSTM, an experimental procedure shown in Fig. 4 was conducted. Four types of trajectories containing diverse patterns are tested. Three evaluation metrics i.e. the Maximum Absolute Error (MAE), the Root Mean Square Error (RMSE) and the Normalized Root Mean Square Error (NRMSE) were used to evaluate the performance of the LSTM controllers [18]. For each test trajectory, the validation procedure shown in Fig. 4 was repeated five times. The $\overline{MAE}$, $\overline{RMSE}$, and $\overline{NRMSE}$ represent the average value of the three metrics across the five attempts. The designed test trajectories as well as the control results of both the control-LSTM and the iDRDPI model have been summarized in Fig. 5a-d and will be described next:

A. Response on descending sinusoidal trajectory

A descending sinusoidal trajectory (6) with $f = 0.3$ and $\tau = 0.05$ is generated as:

$$\theta(t) = Ae^{-\tau t}(\sin(2\pi ft - \frac{\pi}{2}) + 1), \qquad [\text{deg}] \qquad (6)$$

with amplitude A set to 10. In terms of the RMSE and NRMSE, the control-LSTM (0.36° and 1.95%) achieves a better performance than the iDRDPI model (1.69° and 9.17%). The control-LSTM drops too fast after the peaks, which leads to an MAE of 1.60°. This can be explained by the fact that the control-LSTM over-compensates for the dead zone at the top of the hysteresis curve. The iDRDPI model produces large offsets with respect to the set trajectory in the unloading phase. Figure 5e plots the actual bending angle versus the desired bending angle. A perfect compensation would lead to a straight line under 45 degrees. The figure shows how the LSTM controller produces a quasi-linear relation, whereas the iDRDPI model compensates the hysteresis to a lesser extent.

B. Response on time-varying frequency trajectory

The performance of the control-LSTM on a trajectory with time-varying frequency is worth investigating. A pressure signal following (7) with $A = 10$, $B = 8$, $f = 0.5$, $\tau = 0.05$, and $c = -0.015$ was utilized to generate an attenuated down-chirp sinusoidal trajectory with shifted baseline:

$$\theta(t) = Ae^{-\tau t}(\sin(2\pi(f + ct)t - \frac{\pi}{2}) + 1) + B. \qquad [\text{deg}] \quad (7)$$

The error of the iDRDPI fluctuates periodically (Fig. 5b). Compared to the control-LSTM, the iDRDPI fails to accurately predict the peak and under-compensates in the unloading phase. This leads to the large RMSE (2.46°) and MAE (4.89°) of the iDRDPI. The error of control-LSTM remains low, achieving an RMSE of 0.58°. However, the error grows as the frequency decreases.

C. Response on period-ascending trajectory

The third test trajectory is a period-ascending trajectory. Following (8), with $A = 6$, $f = 0.3$, $\tau = -0.02$ and $c = 0.005$, an ascending up-chirp sinusoidal trajectory is generated through:

$$\theta(t) = Ae^{-\tau t}(\sin(2\pi(f + ct)t - \frac{\pi}{2}) + 1). \qquad [\text{deg}] \qquad (8)$$

The iDRDPI model performs poorly in the unloading phase (Fig. 5c). In contrast, the NRMSE and MAE of the control-LSTM are 1.82% and 1.32°, respectively, 82.8% and 70.5% better than the iDRDPI in terms of these two metrics.

D. Response on arbitrary trajectories

In practice trajectories most likely vary in a random fashion. Thus arbitrarily varying trajectories have been tested to explore the versatility of the control-LSTM. In addition, some high-frequency small-amplitude variations are added. Such variations could, for example, arise if one wants to compensate

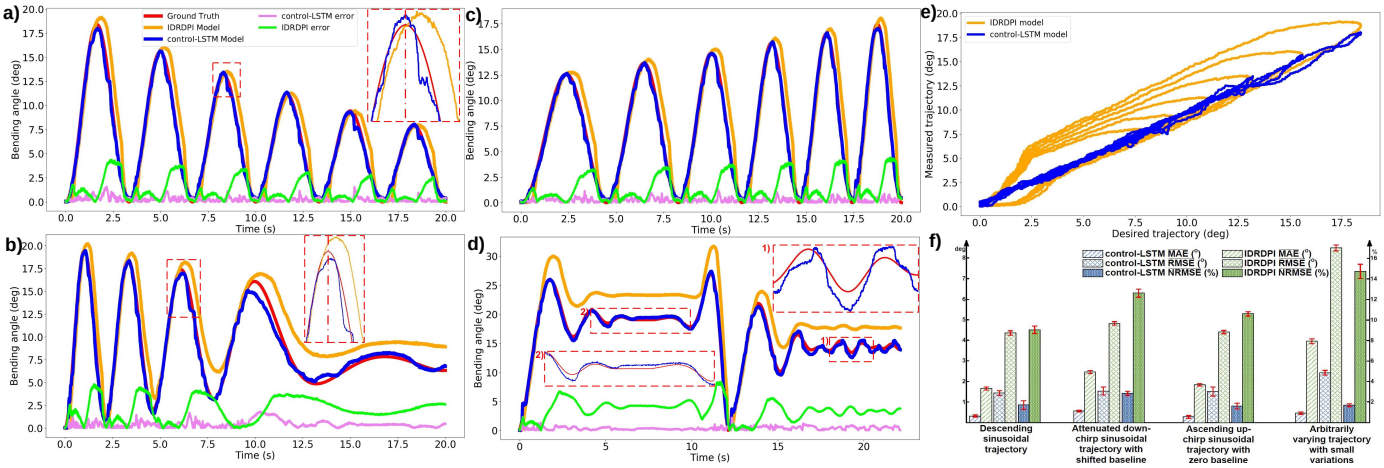

Figure 5. Validation of control-LSTM versus iDRDPI: (a)-(d) the performance of the control-LSTM (blue) and the iDRDPI model (orange) in one out of five attempts on four types of trajectories; (e) relation between desired trajectory (same as in Fig. 5a) and measured trajectory. The LSTM-based controller provides an identity mapping between desired trajectory and measured trajectory after compensation. However, the iDRDPI model-based controller does not fully compensate for the hysteresis; (f) The $\overline{MAE}$ (°), $\overline{RMSE}$ (°) and $\overline{NRMSE}$ (%) of the two controllers on four trajectories.

for vessel deformations induced by heartbeat or blood-flow. In such case, to avoid contact with vessel walls, the catheter may need to perform high-frequency small-amplitude movements.

In general, the error of the control-LSTM is consistently very small, also in regions with small fluctuations (1st close-up in Fig. 5d). It is worth noticing that the control-LSTM is able to follow the set trajectory with high precision in the left plateau region as well (2nd close-up in Fig. 5d). These confirm the small RMSE of $0.46°$ and MAE of $2.41°$ achieved by the control-LSTM. Contrary to this, the iDRDPI shows its worst performance among the four tested trajectories by consistently generating an offset from the set trajectory. Moreover, in the region of small variations, the iDRDPI model does not respond to small fluctuations like the control-LSTM, but rather produces a plateau.

E. Discussion of results

The average inference time of the control-LSTM for a single output point is approximately 25 ms, thus it could be used in a real-time controller. Figure 5f summarizes and compares the performance of both controllers quantitatively based upon the three metrics. Also the standard deviation is given. In terms of NRMSE, the control-LSTM outperforms the iDRDPI model by 80.9%, 77.2%, 84.5%, and 88.3% in the four trajectories. The small standard deviations represented by the error bars in Fig. 5f reveal high repeatability accross experiments. In cardiovascular interventions, the acceptable precision range is generally $1-3$mm [30], [31], albeit sometimes specific scenarios may require better precision. This $1-3$ mm (in displacement) can be converted to $2.09° - 6.26°$ (in bending angle) using the formula introduced in [18], so in this regard, the controller based on the control-LSTM can meet the clinical requirements in terms of precision. This precise LSTM controller opens up new opportunities for lowering interaction forces as is shown in the next section.

V. Validation of the Compliant Motion Controller

A. Experimental setup for validating the compliant controller

A steerable catheter (Fig. 6a) was used to demonstrate compliant motion control capability. Compared to the catheter

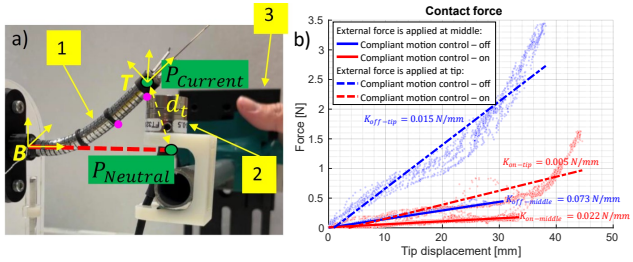

Figure 6. (a) Experimental setup to validate the compliant motion controller: 1. fluidics-driven catheter; 2. F/T sensor; 3. XYZ linear translation stage. The magenta circle shown the contact position in two experiments. (b) Measured force versus displacement of the catheter tip in case external force is applied at the tip (dashed line) and at the middle (solid line) of the catheter.

introduced in Sec. III-A, a 6 mm diameter catheter was used to facilitate contact with a force sensor. Apart from the diameter, structure and working principle remained the same as the catheter from Sec. III-A. As shown in Fig. 6a, an F/T sensor (Nano17, ATI Industrial Automation, USA) attached to an XYZ linear translation stage was used to push the catheter tip in one direction, simulating unknown interaction forces with a vessel or heart wall. During the experiments, the contact force from the F/T sensor and the displacement of the catheter tip measured by the EM sensor in the tip, were recorded.

B. Compliant motion control experiments

Two experiments were conducted. In the first experiment, contact was made at the tip. In the second experiment, contact acted at half the length of the catheter. Each experiment began with the catheter in a straight configuration. The catheter was pushed by the F/T sensor until the muscle reaches maximal pressure (5 bar) to avoid contact force. The displacement was then reversed. Both experiments were conducted first without and then with the compliant motion controller.

In the conducted experiments, the LSTM controller, presented in Sec. III-D, was used. The position controller ran at 40 Hz. Unlike in Sec. IV, where the bending angle was used as input for the LSTM controller, here the tip displacement d_t was used. The tip displacement is the Euclidean distance

between the catheter tip when unloaded $P_{Neutral}$ to the current tip position $P_{Current}$ (Fig. 6a). Note that the displacement is related to the bending angle, but it is a value that is more convenient to derive from the EM sensor. The displacement was used as input to the LSTM controller to estimate the appropriate pressure needed to pressurize the catheter to the current position (Fig. 2). Forces were measured at 1 kHz, but then subsampled to allow for synchronization with the EM displacement data. Synchronization was done offline.

C. Results

Figure 6b show the measured force versus the tip displacement when an external force is applied at the tip and half along the catheter length. The blue lines show the measured forces when the compliant motion controller was not active. The red lines depict forces when the controller was operational. To evaluate the efficiency of the proposed compliant motion controller, the perceived tip stiffness without (K_{Off}) and with (K_{On}) compliant motion controller were compared. Tip stiffness is measured as the ratio of the applied force versus the tip displacement. When the compliant controller is active, the tip stiffness was reduced by approximately 66% from 0.015 N/mm to 0.005 N/mm. Similarly, tip stiffness decreased from 0.073 N/mm to 0.022 N/mm (around 70%) when the external force acted on the catheter body.

D. Discussion of compliant-motion results

The complex relation revealed in Fig. 6b can be attributed to the fact that the force sensor slipped somewhat along the catheter length during the experiments. Although zero-force was targeted, the interaction force in Fig. 6b did not go down all the way to zero. The following reasons are expected to cause this: 1) in fact, as the catheter bends, the force applied by the F/T sensor will get both a tangential and a radial component. Only the radial force component is actually minimized by the here described compliant motion controller; 2) the control-LSTM based controller is not flawless, errors on that controller will cause some deviation as well; 3) the employed valve has limited bandwidth as well, so it can not react and instantaneously compensate an external force.

Nevertheless, the conducted experiments show that the proposed compliant motion controller can help reduce the force acting at different places along the catheter length. Reductions of approximately 70% can be observed. This proves that deriving highly complex models that describe the mechanical behavior of the catheter is in fact not necessary for these kinds of tasks. Moreover, the proposed approach requires only one sensor to measure the catheter tip pose compared to other more complex methods [3], [4], [8], [32]. Even though the algorithm was only validated in a single bending plane, considering that the catheter can be rotated around its axis and has identical mechanical properties in each bending plane, the algorithm works for single contacts in other directions as well.

VI. Phantom study

A. Experimental setup and experimental procedure

The proposed compliant motion controller is further validated in an aortic phantom (Fig.7a). The phantom features the ascending aorta, aortic arch, and descending aorta. The phantom is made of wood and is manufactured with laser cutting after projecting a real aortic model onto a 2D plane. The phantom was connected on top of the F/T sensor (see inset of Fig.7a) so as to measure the force applied by the catheter on the vessel wall. A catheter, with one steerable segment and several passive segments, called 3Flex [33] is employed in this study. A camera (Allied Vision Technologies GmbH, Germany) is installed directly above the phantom to record the catheter motion. Two EM sensors are embedded at the tip and at the base of the first catheter segment. The 3Flex catheter is inserted from descending aorta, crosses the aortic arch, and is stopped until reaching the aortic root. Afterwards, the catheter is retracted. The above procedure is carried out both with and without employing the compliant motion controller.

B. Results and discussion

During insertion, the average force and maximum force achieved by compliant motion control are 0.14 N and 0.43 N, respectively, which are 65.8% and 70.7% lower than without compliant motion control (Fig. 7b). The catheter can bend to reduce interaction force and move smoothly until reaching the aortic root. On the contrary, when the proposed controller is off, the catheter is stuck in the aortic arch with its tip directly puncturing the vessel wall (see multimedia material attached to this paper). During retraction, the catheter can even not be retracted without the compliant motion control, causing a maximum force of 0.73 N. When the compliant motion control is running, the catheter can be retracted without too much effort, while maintaining the interaction force below 0.44 N. This is 40.0% lower than without the controller running. The results also showed that the method could reduce the user's mental load as the user does not need to focus on the force control, which allows them to pay more attention to high-level tasks such as decision making. In addition, a reduction in the procedure duration is also observed with the proposed method.

VII. Conclusion

This work introduced a deep-learning-based compliant motion controller for a robotic catheter. Such a controller can actively bend the catheter tip away from the environment such that excessive interaction forces can be automatically avoided. This feature could contribute to safer interventions. The proposed method only requires sensors that measure the tip pose. The approach is simple and does not necessitate complex sensors that measure distributed contacts or that measure the input torque applied by the actuators. The proposed compliant motion controller features a tip position controller based on a control-LSTM. This work shows how the control-LSTM was able to compensate for rate-dependent, saturated and asymmetric hysteresis present in the catheter system. Based on this tip position controller, a compliant motion controller was proposed. Experiments both in a simplified setup as well in an aortic phantom showed how catheter contact forces could be reduced by approximately 70%. Although showcased on a pneumatically-driven catheter, this method is believed to be transferable to other actuation methods such as cable-driven with moderate extra efforts. This work shows that it is not

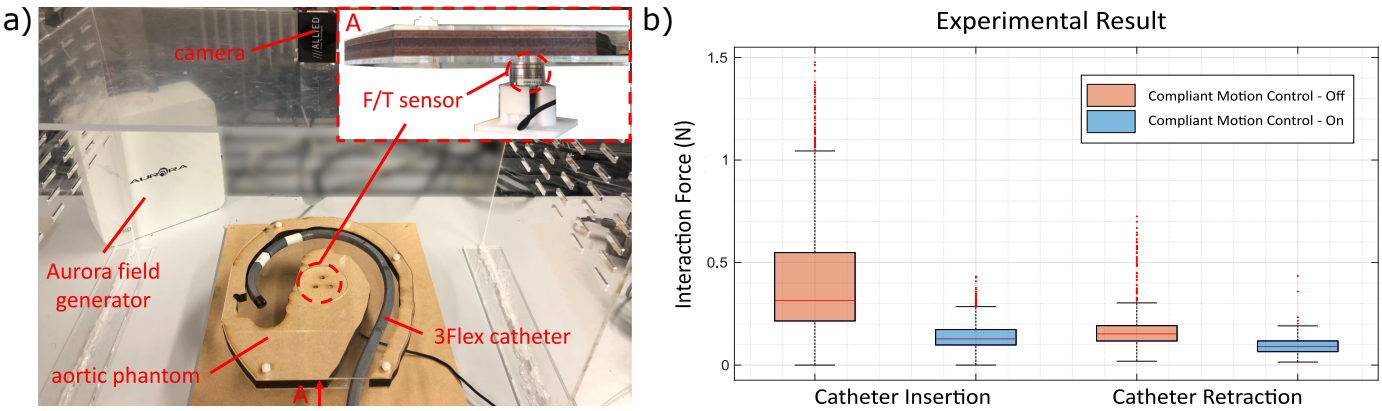

Figure 7. Phantom study: a) a setup contains catheter, aortic phantom, F/T sensor, camera and EM tracking system; b) interaction force shown in a box plot.

always necessary to elaborate complex mechanic models to steer robotic catheters.

ACKNOWLEDGMENT

The authors would like to thank Saeid Shakiba for his helpful advice on the DRDPI model.

REFERENCES

[1] T. da Veiga *et al.*, "Challenges of continuum robots in clinical context: A review," *Prog. in Biomed. Eng.*, vol. 2, no. 3, p. 032003, 2020.

[2] S. B. Kesner and R. D. Howe, "Force control of flexible catheter robots for beating heart surgery," in *2011 IEEE International Conference on Robotics and Automation (ICRA)*, 2011, pp. 1589–1594.

[3] M. Mahvash and P. E. Dupont, "Stiffness control of surgical continuum manipulators," *IEEE Trans. on Robot.*, vol. 27, no. 2, pp. 334–345, 2011.

[4] R. E. Goldman, A. Bajo, and N. Simaan, "Compliant motion control for multisegment continuum robots with actuation force sensing," *IEEE Transactions on Robotics*, vol. 30, no. 4, pp. 890–902, 2014.

[5] G. Ji, J. Yan, J. Du *et al.*, "Towards safe control of continuum manipulator using shielded multiagent reinforcement learning," *IEEE Robotics and Automation Letters*, vol. 6, no. 4, pp. 7461–7468, 2021.

[6] M. C. Yip and D. Camarillo, "Model-less feedback control of continuum manipulators in constrained environments," *IEEE Transactions on Robotics*, vol. 30, no. 4, pp. 880–889, 2014.

[7] M. C. Yip *et al.*, "Model-less hybrid position/force control: a minimalist approach for continuum manipulators in unknown, constrained environments," *IEEE Robot. and Automat. Lett.*, vol. 1(2), pp. 844–851, 2016.

[8] D. Jakes, Z. Ge, and L. Wu, "Model-less active compliance for continuum robots using recurrent neural networks," *2019 IEEE/RSJ International Conference on Intelligent Robots and Systems (IROS)*, 2019.

[9] M. Azizkhani, I. S. Godage, and Y. Chen, "Dynamic control of soft robotic arm: A simulation study," *IEEE Robot. and Automat. Lett.*, vol. 7, no. 2, pp. 3584–3591, 2022.

[10] B. Bardou *et al.*, "Improvements in the control of a flexible endoscopic system," in *IEEE Conf. on Robot. and Automat.*, 2012, pp. 3725–3732.

[11] B. Yu *et al.*, "Probabilistic kinematic model of a robotic catheter for 3d position control," *Soft Robotics*, vol. 6, pp. 184–194, 2019.

[12] D. Baek *et al.*, "Hysteresis compensator with learning-based hybrid joint angle estimation for flexible surgery robots," *IEEE Robot. and Automat. Lett.*, vol. 5, no. 4, pp. 6837–6844, 2020.

[13] T. N. Do *et al.*, "Hysteresis modeling and position control of tendon-sheath mechanism in flexible endoscopic systems," *Mechatronics*, vol. 24, no. 1, pp. 12–22, 2014.

[14] O. M. Omisore, S. P. Han, L. X. Ren, G. S. Wang, F. L. Ou, H. Li, and L. Wang, "Towards characterization and adaptive compensation of backlash in a novel robotic catheter system for cardiovascular interventions," *IEEE Trans. on Biomed. Circuits and Syst.*, vol. 12, pp. 824–838, 2018.

[15] S. Shakiba *et al.*, "Tracking control of an sma-driven actuator with rate-dependent behavior using an inverse model of hysteresis," *J. of the Brazilian Soc. of Mech. Sci. and Eng.*, vol. 42, 2020.

[16] R. A. Porto *et al.*, "Position control of medical cable-driven flexible instruments by combining machine learning and kinematic analysis," in *IEEE Int. Conf. on Robot. and Automat. (ICRA)*, 2019, pp. 7913–7919.

[17] W. Xu, J. Chen, H. Y. Lau, and H. Ren, "Data-driven methods towards learning the highly nonlinear inverse kinematics of tendon-driven surgical manipulators," *The Int. J. of Med. Robot. and Comput. Assisted Surgery*, vol. 13, no. 3, p. e1774, 2017.

[18] D. Wu *et al.*, "Hysteresis modeling of robotic catheters based on long short-term memory network for improved environment reconstruction," *IEEE Robot. and Automat. Lett.*, vol. 6, no. 2, pp. 2106–2113, 2021.

[19] S. Shakiba *et al.*, "Modeling and compensation of asymmetric rate-dependent hysteresis of a miniature pneumatic artificial muscle-based catheter," *Mech. Syst. and Signal Process.*, vol. 154, p. 107532, 2021.

[20] I. D. Walker, "Continuous backbone "continuum" robot manipulators," *International Scholarly Research Notices*, vol. 2013, 2013.

[21] B. A. Jones and I. D. Walker, "Kinematics for multisection continuum robots," *IEEE Transactions on Robotics*, vol. 22, no. 1, pp. 43–55, 2006.

[22] M. Wagner *et al.*, "4d interventional device reconstruction from biplane fluoroscopy," *Medical physics*, vol. 43, no. 3, pp. 1324–1334, 2016.

[23] J. Avery *et al.*, "Shape sensing of variable stiffness soft robots using electrical impedance tomography," in *2019 IEEE Inter. Conf. on Robot. and Automat. (ICRA)*, 2019, pp. 9066–9072.

[24] G. Gerboni *et al.*, "Feedback control of soft robot actuators via commercial flex bend sensors," *IEEE/ASME Trans. on Mechatronics*, vol. 22, no. 4, pp. 1881–1888, 2017.

[25] X. T. Ha *et al.*, "Robust catheter tracking by fusing electromagnetic tracking, fiber bragg grating and sparse fluoroscopic images," *IEEE Sensors Journal*, vol. 21, no. 20, pp. 23 422–23 434, 2021.

[26] X. T. Ha, D. Wu, C.-F. Lai *et al.*, "Contact localization of continuum and flexible robot using data-driven approach," *IEEE Robot. and Automat. Lett.*, vol. 7, no. 3, pp. 6710–6917, 2022.

[27] A. Devreker *et al.*, "Fluidic actuation for intra-operative in situ imaging," in *2015 IEEE/RSJ International Conference on Intelligent Robots and Systems (IROS)*. IEEE, 2015, pp. 1415–1421.

[28] V. Hassani, T. Tjahjowidodo, and T. N. Do, "A survey on hysteresis modeling, identification and control," *Mech. syst. and signal process.*, vol. 49, no. 1-2, pp. 209–233, 2014.

[29] S. Hochreiter and J. Schmidhuber, "Long short-term memory," *Neural computation*, vol. 9, no. 8, pp. 1735–1780, 1997.

[30] H. Nijland *et al.*, "Evaluation of accuracy and precision of ct-guidance in radiofrequency ablation for osteoid osteoma in 86 patients," *PLoS One*, vol. 12, no. 4, p. e0169171, 2017.

[31] O. Al-Ahmad *et al.*, "Improved fbg-based shape sensing methods for vascular catheterization treatment," *IEEE Robotics and Automation Letters*, vol. 5, no. 3, pp. 4687–4694, 2020.

[32] R. E. Goldman, A. Bajo, and N. Simaan, "Compliant motion control for continuum robots with intrinsic actuation sensing," in *2011 IEEE Int. Conf. on Robot. and Automa. (ICRA)*. IEEE, 2011, pp. 1126–1132.

[33] M. H. D. Ansari *et al.*, "Proof-of-concept medical robotic platform for endovascular catheterization," in *11th Conf. on New Technologies for Computer and Robot Assisted Surgery (CRAS)*, 2022, pp. 66–67.